

Antiferromagnetic ground state of La_2CuO_4 : A parameter-free *ab initio* descriptionChristopher Lane,^{1,*} James W. Furness,² Ioana Gianina Buda,¹ Yubo Zhang,² Robert S. Markiewicz,¹ Bernardo Barbiellini,^{3,1} Jianwei Sun,^{2,†} and Arun Bansil^{1,‡}¹*Physics Department, Northeastern University, Boston, Massachusetts 02115, USA*²*Department of Physics and Engineering Physics, Tulane University, New Orleans, Louisiana 70118, USA*³*Department of Physics, School of Engineering Science, Lappeenranta University of Technology, FI-53851 Lappeenranta, Finland*

(Received 27 November 2017; revised manuscript received 30 August 2018; published 25 September 2018)

We show how an accurate first-principles treatment of the antiferromagnetic ground state of La_2CuO_4 can be obtained without invoking any free parameters such as the Hubbard U . The magnitude and orientation of our theoretically predicted magnetic moment of $0.495\mu_B$ on Cu sites along the (100) direction are in excellent accord with experimental results. The computed values of the band gap (1.00 eV) and the exchange coupling (-138 meV) match the corresponding experimental values. We identify interesting band splittings below the Fermi energy, including an appreciable Hund's splitting of 1.25 eV. The magnetic form factor obtained from neutron scattering experiments is also well described by our calculations. Our study thus opens up a pathway for first-principles investigations of electronic and atomic structures and phase diagrams of cuprates and other complex materials.

DOI: [10.1103/PhysRevB.98.125140](https://doi.org/10.1103/PhysRevB.98.125140)**I. INTRODUCTION**

A fundamental challenge that has remained unsolved ever since the discovery of high- T_c superconductivity in hole-doped La_2CuO_4 nearly 30 years ago has been that a first-principles description of the ground-state electronic structure of La_2CuO_4 has not been possible. The magnetic state of La_2CuO_4 , in particular, has been especially hard to capture within a uniform theoretical picture. Various attempts within the Hohenberg-Kohn-Sham [1,2] density functional theory (DFT) framework have at best yielded mixed results [3]. In particular, most studies have struggled to model correctly the antiferromagnetic (AFM) ground state of La_2CuO_4 , and have therefore been unable to provide a handle on the key experimentally observed properties of this parent compound, which gives birth to the novel phenomena of high- T_c superconductivity.

More specifically, the local-spin-density approximation (LSDA) [4,5] incorrectly predicts La_2CuO_4 and other half-filled cuprates to be nonmagnetic (NM) metals [3,6–8], in complete disagreement with experimental findings. The generalized gradient approximation (GGA) [9] only produces a weak AFM order [10]. While Hartree-Fock captures the AFM ground state and the magnetic form factor, the computed band gap of ≈ 17 eV is far too large [11,12], and the strength of the exchange coupling is too small by a factor of 4 [13].

Failure of the DFT in capturing the AFM state of half-filled cuprates has led to the widely held belief that DFT is fundamentally limited in its reach for addressing electronic structures of cuprates and many other classes of important materials. The development of methods, which incorporate

stronger electron correlations in order to stabilize the AFM ground state, has been effective in describing the low-energy spectra of the cuprates. These include “beyond DFT” schemes for extending the DFT into the intermediate coupling regime [14] such as the quasiparticle GW (QP-GW) and various dynamical mean-field theory (DMFT) based schemes [15–17]. All beyond DFT schemes, however, require the introduction of empirically derived, *ad hoc* parameters, which compromise their predictive power.

Following the theorems of Hohenberg-Kohn and Kohn-Sham, there must exist an exact exchange-correlation energy (E_{xc}) functional that incorporates *all* many-body effects into an effective single-particle Hamiltonian [1,2,18]. This would allow an exact *ab initio* treatment of all materials, including strongly correlated systems, at least insofar as the ground-state energy and the related physical properties are concerned. As we invoke improved approximations to the exchange-correlation functional, we can then also expect concomitant improvements in the DFT predictions of the ground-state properties [19].

Recently, the strongly constrained and appropriately normed (SCAN) meta-GGA exchange-correlation functional [20], which obeys all known constraints applicable to a meta-GGA functional [21], has shown promise [22] by significantly improving the description of diversely bonded systems. These include surface properties of metals [23], ice [24] and liquid water [25], subtle structural distortions in ferroelectrics [26,27], and transitions from insulator and semiconducting to metallic phases [24,28].

In this paper, we show how electronic, geometric, and magnetic structures of La_2CuO_4 can be captured accurately by SCAN meta-GGA [20] within the DFT framework. Our first-principles, parameter-free magnetic ground state obtained in this way reproduces the key experimentally observed properties of La_2CuO_4 . These include the magnitude and orientation of the local magnetic moment on copper sites, size of the

*c.lane@neu.edu

†jsun@tulane.edu

‡ar.bansil@neu.edu

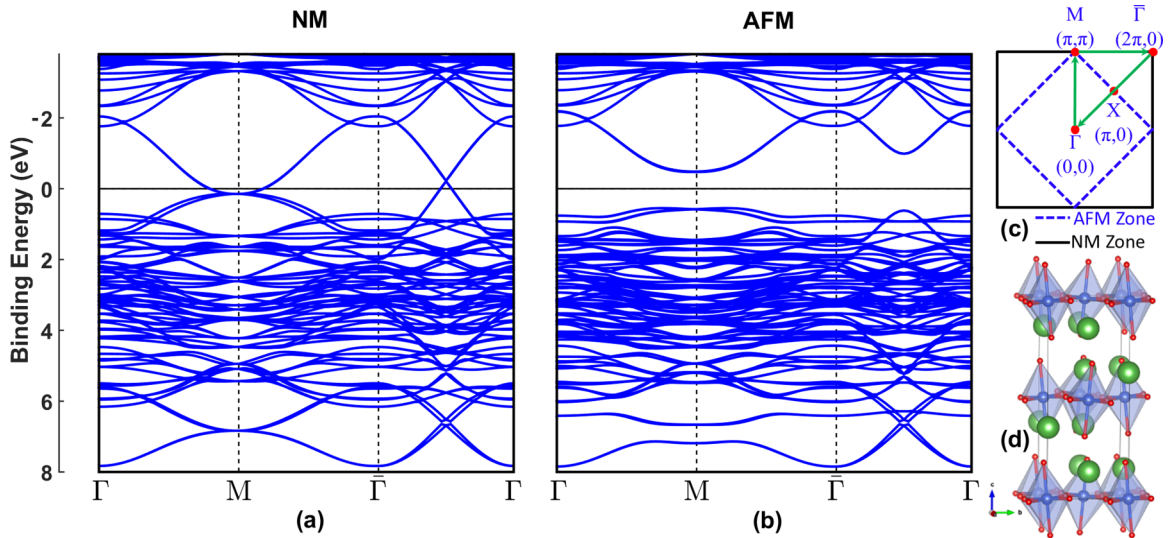


FIG. 1. (a), (b) Electronic band dispersions of La_2CuO_4 in the LTO crystal structure for the nonmagnetic (NM) and antiferromagnetic (AFM) phases. (c) A schematic of the NM and AFM Brillouin zones; where the path followed in the electronic dispersions in (a) and (b) is marked. (d) Crystal structure of La_2CuO_4 in the LTO phase with copper, oxygen, and lanthanum atoms represented by blue, red, and green spheres, respectively.

optical band gap, strength of the exchange coupling, and the shape of the magnetic form factor. The accuracy of these predictions reflects the systematic improvement in the exchange-correlation energy embodied in the SCAN functional.

II. COMPUTATIONAL DETAILS

Ab initio calculations were carried out by using the pseudopotential projector augmented-wave (PAW) method [29] implemented in the Vienna *ab initio* simulation package (VASP) [30,31] with an energy cutoff of 500 eV for the plane-wave basis set. Exchange-correlation effects were treated using the SCAN meta-GGA scheme [20], where a $12 \times 12 \times 6$ Γ -centered k -point mesh was used to sample

the Brillouin zone. Spin-orbit coupling effects were included self-consistently. We used the low-temperature orthorhombic (LTO) crystal structure of $Bmab$ symmetry in accord with the experimentally observed structure of La_2CuO_4 [28,32,33]. All sites in the unit cell along with the unit cell dimensions were relaxed using a conjugate gradient algorithm to minimize energy with an atomic force tolerance of $0.008 \text{ eV}/\text{\AA}$ and a total energy tolerance of 10^{-5} eV . The theoretically obtained structural parameters are in good accord with the corresponding experimental results (see Appendix C for details). As shown in Fig. 1(d), the LTO structure can be viewed as being a $\sqrt{2} \times \sqrt{2}$ body-centered-tetragonal superlattice of $I4/mmm$ symmetry in which $a' \approx b' \approx \sqrt{2}a$; the CuO_6 octahedra are rotated along the (110) and $(1\bar{1}0)$ directions in alternate layers.

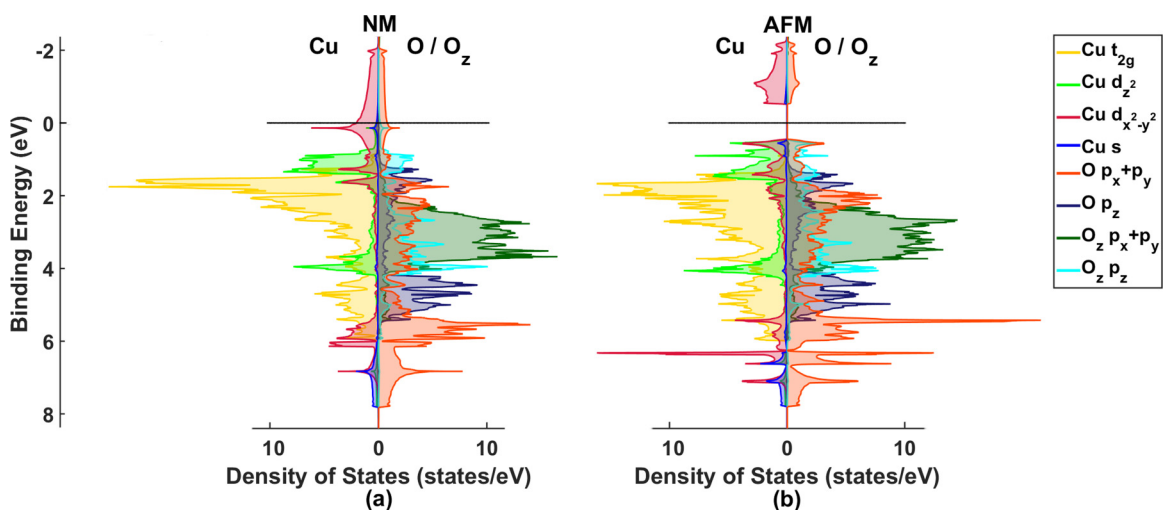


FIG. 2. Site-resolved partial densities of states in the nonmagnetic (NM) and antiferromagnetic (AFM) states of La_2CuO_4 in the LTO structure. Copper and oxygen characters are plotted on the left- and right-hand sides, respectively. Shadings and lines of various colors (see legend) give contributions from various orbitals of copper, apical (O_z), and in-plane (O) oxygen sites.

III. ELECTRONIC STRUCTURE OF La_2CuO_4

Figures 1(a) and 2(a) show the band structure and partial densities of states (PDOSs) associated with various Cu and O orbitals in the NM phase [34]. Here, and throughout, we will distinguish the in-plane oxygen atoms from the apical oxygen atoms as O and O_z , respectively. We see that the half-filled antibonding Cu $d_{x^2-y^2}/O$ $p_x + p_y$ band crosses the Fermi level and that its bonding partner “bookends” the PDOS from the bottom over binding energies of 6–8 eV; see Appendix F for various orbital contributions to the band structure. The orbital character at the Fermi level is predominantly (70%) Cu $d_{x^2-y^2}$, with O $p_x + p_y$, Cu d_{z^2} , O_z p_z , and Cu s sharing the remaining (30%) weight. On the other hand, at a binding energy of 6.8 eV, the character is mainly O $p_x + p_y$ (52%), Cu $d_{x^2-y^2}$ (19%), and Cu $4s$ (14%). The preceding results are similar to what we would expect from a molecular-bonding-type picture of an octahedrally coordinated metal [35,36]. Note that due to the tetragonal Jahn-Teller distortion of the Cu-O octahedra, the Cu d_{z^2}/O_z p_z antibonding level lies at approximately 1 eV while the related bonding level lies around 4 eV below the Fermi energy. Copper d_{z^2} and apical oxygen p_z have a combined weight of 70% and 60% of the total DOS at 1 and 4 eV, respectively. Remaining states in the crystal-field-split manifold, i.e., the nonbonded oxygen atoms and the hybridized t_{2g} levels, sit at binding energies of 1–6 eV. In comparison to the usual hybridization schematic of Fink *et al.* [37], we highlight the non-negligible presence of Cu d_{z^2} and $4s$ in the molecular-bonding picture of copper and oxygen in Appendix D.

Figures 1(b) and 2(b) show that the AFM state stabilizes with a band gap of approximately 1 eV that opens up around the Fermi energy of the NM system. This gap is in good agreement with optical [11] and transport [12] data. Notably, in estimating the band gap from the optical spectra from the half-filled system given by Uchida *et al.* (see Ref. [11], Fig. 4), we should be careful to look for the leading edge gap in the spectrum, which yields the value of 0.91 eV that is in good accord with our predicted value of 1.0 eV in La_2CuO_4 , excitonic effects notwithstanding. (The first peak in the optical spectrum above the Fermi energy is not a good marker for estimating the band gap.) Note also that the weak midinfrared features in the optical spectra of cuprates, reported in some nominally undoped samples, have been interpreted mainly in terms of residual impurities. Although scanning tunneling spectroscopy (STS) has not been successful on La_2CuO_4 , a large charge gap in good agreement with our results has been observed in STS studies in a closely related cuprate; in-gap features were observed, but only in the vicinity of impurities [38]. Transport studies find similar gap values, suggesting an absence of mobile midinfrared carriers [12,39].

The physical interpretation of the band gap obtained in the ground-state DFT calculations has been the subject of much debate in the literature over the years. In comparing the band structures based on different functionals one must distinguish between the nature of the effective exchange-correlation potential obtained in the Kohn-Sham (KS) and generalized Kohn-Sham (gKS) formalisms underlying the construction of various functionals. KS potentials are “multiplicative” by design in that they are orbital independent. In sharp contrast, gKS potentials are formally constructed with the freedom to be orbital dependent and can thus be “nonmultiplicative.”

TABLE I. Comparison of theoretically predicted magnetic moments and band gaps of the low-temperature orthorhombic (LTO) phase of La_2CuO_4 using various meta-GGA functionals.

Functional	Cu magnetic moment (μ_B)	Band gap (eV)
M06L	Unable to converge due to numerical instabilities	
revTPSS	0.320	0.21
TPSS	0.313	0.18
SCAN	0.490	1.0

In particular, LSDA/GGA band structures involve multiplicative effective potentials, while the current and common SCAN implementations involve nonmultiplicative potentials due to the inclusion of the kinetic energy density as an ingredient, and thus differ in their basic underlying designs.

In this connection, Perdew *et al.* [40] have shown recently that for a given density functional, the gKS band gap is equal to the fundamental band gap in the solid, which is defined as the ground-state energy difference between systems with different numbers of electrons. There is thus a firm basis for comparing computed band gaps within the gKS-based SCAN formalism with the experimentally observed band gaps (excluding excitonic effects). The preceding considerations indicate that as a meta-GGA functional improves the description of the ground state, it will necessarily also lead to improvement in the band gap.

Table I compares the magnetic moments and band gaps of LCO for various meta-GGA DFT functionals. Here we tested popular meta-GGA functionals available in VASP including M06L [41], TPSS [42] and revTPSS [43]. M06L is widely used in chemistry and is heavily parametrized, which leads to well-known numerical stability problems (a consequence of overfitting) [44]. Our calculations confirm this point. TPSS and revTPSS are earlier versions of the nonempirical meta-GGA’s, which are seen to underestimate the magnetic moment, and give only slight improvement over PBE. Overall, the best results are found with SCAN.

The 1-eV gap in the electronic structure develops in the half-filled Cu $d_{x^2-y^2}$ dominated band by splitting the up- and down-spin antibonding bands. Remarkably, as a result of electron-electron interactions, a “mirrored” splitting occurs around 7 eV binding energy in the bonding band, which breaks its spin degeneracy (see orbital contributions to the AFM band structure in Appendix F). The splitting at 7 eV binding energy occurs along the Γ - M - $\bar{\Gamma}$ cut in the Brillouin zone forming a 0.5-eV gap. However, due to the strong O $p_x + p_y$ character along $\bar{\Gamma}$ - Γ , a full gap in the energy spectrum is prevented. A further consequence of this splitting is the generation of a flat (nondispersing) band, exhibiting a strong van Hove singularity in the DOS. Distinct splittings are also generated in the Cu d_{z^2}/O_z p_z bonding and antibonding bands. As a result of splittings in the antibonding d_{z^2} bands, a gap of 0.16 eV forms, seen at 1 eV binding energy along Γ - M in the electronic structure (Fig. 3). Comparing the site-resolved atomic projections (red dots) for Cu $d_{x^2-y^2}$ and Cu d_{z^2} in Fig. 3, the gap at 1 eV is identified as an avoided crossing, where the $d_{x^2-y^2}/d_{z^2}$ band degeneracy is broken in the AFM state. There may be similar splittings within the t_{2g} complex, but these are harder to discern.

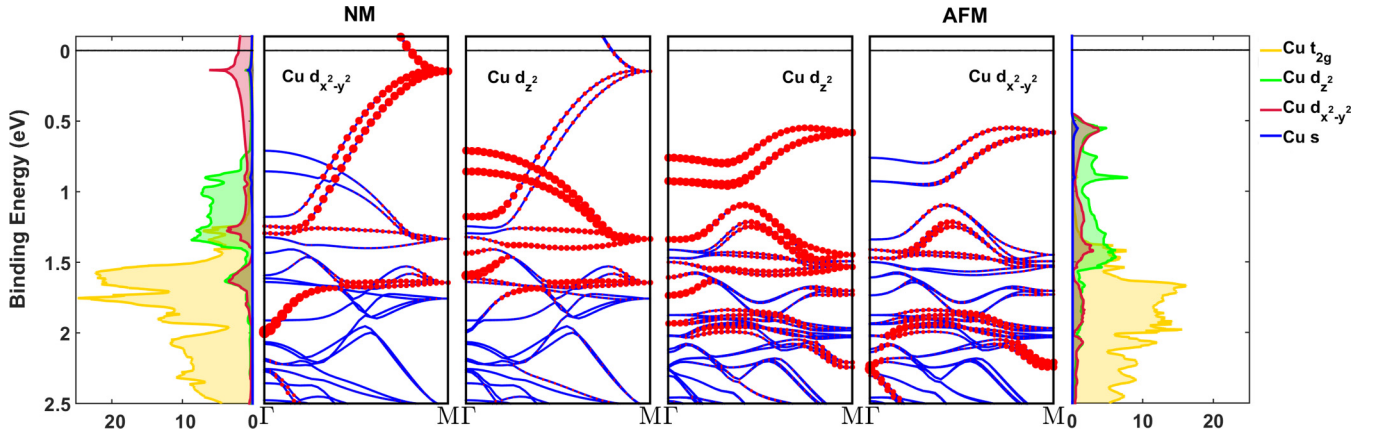


FIG. 3. Electronic band structure (blue lines) of La_2CuO_4 in the LTO structure in the nonmagnetic (NM) and antiferromagnetic (AFM) states, overlaid with site-resolved atomic projections (red dots) for Cu $d_{x^2-y^2}$ and Cu d_{z^2} . The sizes of the red dots are proportional to the fractional weights of the indicated orbitals. The corresponding projected DOS for the NM and AFM states are given at the periphery of the figure on the left- and right-hand sides, respectively.

In the AFM phase, the conduction states are dominated by $d_{x^2-y^2}$ (68%). However, the valence states are not dominated by Cu $d_{x^2-y^2}$, but consist of almost equal contributions (around 0.55 eV binding energy) from $d_{x^2-y^2}/O$ $p_x + p_y$ and d_{z^2}/O_z p_z ($\approx 20\%$ each; 80% of the total weight). The unexpected character of the valence states stems from an appreciable splitting in the d_{z^2}/O_z p_z antibonding level. We emphasize that, due to the sizable d_{z^2} contribution to the valence states, the conventional one-band model of the cuprates is of limited reach [45], as is the classification of the cuprates within the Zaanen-Sawatzky-Allen [46] scheme.

IV. INTRASITE MULTIORBITAL ELECTRON-ELECTRON INTERACTIONS

The aforementioned spin splittings can be seen as a consequence of intrasite multiorbital electron-electron interactions. We can estimate the effective values of the multiorbital interactions from our ground-state electronic structure by mapping a multiorbital Hubbard model [47] to our site-resolved partial densities of states.

Let us first consider an orbital μ in a ligand field. The energy of this orbital will be split into a pair of bonding and antibonding states with energies

$$E_{\pm}^{\mu\sigma} = a_{\mu\sigma}^{\pm} \pm h_{\mu}, \quad (1)$$

where \pm indexes the bonding ($-$) and antibonding ($+$) states, h is the hybridization strength, and $a_{\mu\sigma}^{\pm}$ is the bare

orbital energy. The bare orbital energy can be broken down into two contributions, on-site atomic and electron-electron interactions,

$$a_{\mu\sigma}^{\pm} = E_{\text{atomic}}^{\mu} + H_{\text{int}}^{\mu\sigma\pm}. \quad (2)$$

For the form of $H_{\text{int}}^{\mu\sigma\pm}$ we will follow Oles [47], whereby we only consider electron correlations in the $3d$ orbitals, and the electron-electron interactions are restricted to be intrasite, *à la* Hubbard. In order to make the model tractable, we work in the mean field where an electronic state is influenced by the presence of other electrons via the effective field $H_{\mu\sigma}$,

$$H_{\mu\sigma} = U \langle n_{\mu\bar{\sigma}} \rangle + \sum_{v \neq \mu} U' \langle n_{v\bar{\sigma}} \rangle + \sum_{v \neq \mu} (U' - J_H) \langle n_{v\sigma} \rangle, \quad (3)$$

with orbital (μ, v) and spin ($\sigma, \bar{\sigma} = -\sigma$) indices, and $\langle n_{\mu\sigma} \rangle$ is the average electron occupation for a given state. Therefore, we can insert $H_{\mu\sigma}$ from Eq. (3) into Eq. (2),

$$a_{\mu\sigma}^{\pm} = E_{\text{atomic}}^{\mu} + U \langle n_{\mu\bar{\sigma}}^{\pm} \rangle + U' \sum_{v \neq \mu} \langle n_{v\bar{\sigma}}^{\pm} \rangle + (U' - J_H) \sum_{v \neq \mu} \langle n_{v\sigma}^{\pm} \rangle. \quad (4)$$

Since our main interest is to extract the interaction parameters, i.e., U and J_H , we take the difference between spin configurations and sum over bonding and antibonding states to eliminate the hybridization and atomic contributions, which are assumed to be spin independent, yielding

$$E^{\mu\uparrow} - E^{\mu\downarrow} = \sum_{\pm} E_{\pm}^{\mu\uparrow} - E_{\pm}^{\mu\downarrow} = \sum_{\pm} (a_{\mu\uparrow}^{\pm} - a_{\mu\downarrow}^{\pm}) \quad (5)$$

$$= \sum_{\pm} \left[\left(U \langle n_{\mu\downarrow}^{\pm} \rangle + U' \sum_{v \neq \mu} \langle n_{v\downarrow}^{\pm} \rangle + (U' - J_H) \sum_{v \neq \mu} \langle n_{v\uparrow}^{\pm} \rangle \right) - \left(U \langle n_{\mu\uparrow}^{\pm} \rangle + U' \sum_{v \neq \mu} \langle n_{v\uparrow}^{\pm} \rangle + (U' - J_H) \sum_{v \neq \mu} \langle n_{v\downarrow}^{\pm} \rangle \right) \right] \quad (6)$$

$$= U(N_{\mu\downarrow} - N_{\mu\uparrow}) + U' \sum_{v \neq \mu} (N_{v\downarrow} - N_{v\uparrow}) + (U' - J_H) \sum_{v \neq \mu} (N_{v\uparrow} - N_{v\downarrow}). \quad (7)$$

Here, $N_{\mu\sigma} = \sum_{\pm} \langle n_{\mu\sigma}^{\pm} \rangle$ is the total number of electrons in orbital μ of spin σ .

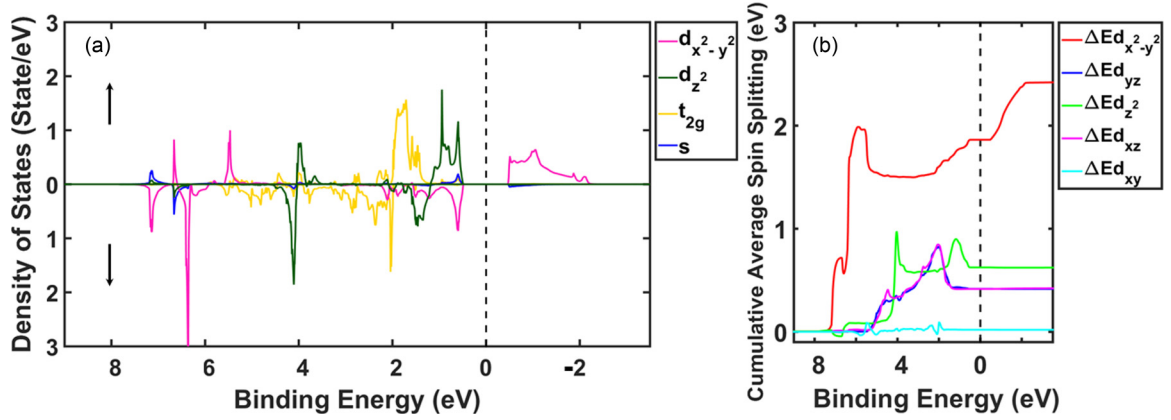


FIG. 4. (a) Single copper site-resolved partial densities of states in the AFM phase of LTO La_2CuO_4 . Copper d -orbital characters are plotted in various colors (see legend). (b) Cumulative average spin-splitting energies calculated for various d orbitals for a single copper site.

After hybridization, energy levels $E^{\mu\sigma}$ need not be localized in energy and may be smeared. With this in mind, we interpret $E^{\mu\sigma}$ as the average level energy, and write $E^{\mu\sigma}$ with respect to the density of states as

$$E^{\mu\sigma} = \int_W g_{\mu\sigma}(e) e de, \quad (8)$$

where W is the bandwidth. Moreover, $E^{\mu\uparrow} - E^{\mu\downarrow}$ can be written as

$$E^{\mu\uparrow} - E^{\mu\downarrow} = \int_W [g_{\mu\uparrow}(e)e - g_{\mu\downarrow}(e)e] de. \quad (9)$$

Thus, we arrive at a linear set of equations indexed by μ relating the average orbital spin splitting and the mean-field multiorbital interactions,

$$\begin{aligned} & \int_W [g_{\mu\uparrow}(e)e - g_{\mu\downarrow}(e)e] de \\ &= U(N_{\downarrow} - N_{\uparrow}) + U' \sum_{v \neq \mu} (N_{v\downarrow} - N_{v\uparrow}) \\ &+ (U' - J_H) \sum_{v \neq \mu} (N_{v\uparrow} - N_{v\downarrow}). \end{aligned} \quad (10)$$

Specifically, using the copper-atom-projected partial density of states in the AFM phase of LTO La_2CuO_4 in Fig. 4(a), we find $N_{d_{x^2-y^2}\downarrow} - N_{d_{x^2-y^2}\uparrow} = 1/2$, and 0 for all other orbitals [using $\int de \sum_{\sigma} g_{\mu\sigma}(e)$ normalized to 1.0]. This significantly simplifies Eq. (10) to

$$\int_W g_{d_{x^2-y^2}\uparrow}(e)e - g_{d_{x^2-y^2}\downarrow}(e)e de = U/2, \quad (11)$$

$$\int_W g_{(\mu \neq d_{x^2-y^2})\uparrow}(e)e - g_{(\mu \neq d_{x^2-y^2})\downarrow}(e)e de = U'(1/2) + (U' - J_H)(-1/2) = J_H/2. \quad (12)$$

Furthermore, we compute $\int_W g_{\mu\uparrow}(e)e - g_{\mu\downarrow}(e)e de$ for each orbital [cumulative sum shown in Fig. 4(b)]. The average splitting calculated for $d_{x^2-y^2}$, d_{z^2} , d_{yz} , d_{xz} , and d_{xy} is 2.423, 0.624, 0.424, 0.424, and 0.0195 eV, respectively [48]. Interestingly, we find a strong orbital dependence of the spin splitting. Using our first-principles splittings, we estimate U

as 4.846 eV. In estimating J_H we take the largest splitting as an upper bound on J_H , and obtain J_H as 1.248 eV. The fact that we find a substantial Hund's splitting is important for building accurate low-energy models of the electronic structure. These values are in line with Jang *et al.* [49] and suggest that La_2CuO_4 is closer to a Slater-type insulator in agreement with Comanac *et al.* [50] and $\text{SU}(2)$ spin models [51].

V. MAGNETIC SPIN STRUCTURE

Figure 5 shows our theoretically obtained AFM structure within the LTO unit cell, where red and blue arrows denote copper and apical oxygen magnetic moments, respectively. The predicted value of the magnetic moment on copper sites is $0.495\mu_B$ [52], which is in accord with the corresponding experimental value of $0.60 \pm 0.05\mu_B$ [53,54] (see Appendix E for a discussion of experimental values). Moreover, the copper magnetic moment vector in Fig. 5 clearly displays the planar Ising AFM ordering along the (100) axis as seen in low-temperature experimental studies [55]. Our calculations show that the delicate 2° out-of-plane spin tilt [55,56] is energetically indistinguishable from the 0° orientation. The pinning of the moment vector with respect to the lattice would not be possible without the inclusion of spin-orbit coupling [57]. We obtain a small moment ($0.01\mu_B$) on the apical oxygens (blue), which is anticollinear to that of copper atoms lying at the centers of the octahedra. The in-plane oxygen atoms exhibit spin polarization but no net magnetic moment. Here, the SCAN functional better captures the subtle effects of many-body interactions and hybridizations in the solid state environment compared to previous semilocal functionals [58].

VI. EXCHANGE COUPLING

In order to determine the strength of the exchange coupling, we map the total energies of the AFM and FM phases onto those of the nearest-neighbor spin- $\frac{1}{2}$ Heisenberg Hamiltonian in the mean-field approximation [13,59,60]. For La_2CuO_4 , the Heisenberg Hamiltonian gives a reasonable description of the low-lying excitations, and thus a good estimate of the Heisenberg exchange parameter J [55]. In the mean-field limit, the difference in total energies of the FM and

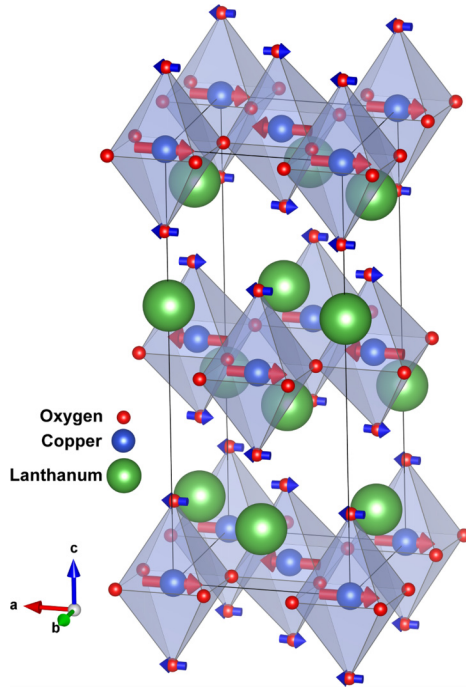


FIG. 5. Theoretically predicted AFM state of La_2CuO_4 in the LTO crystal structure. Red and blue arrows represent copper and apical oxygen magnetic moments, respectively; in-plane oxygen atoms have no net magnetic moment. Octahedral faces are shaded in blue; black lines mark the unit cell.

AFM phases is

$$\Delta E = E_{\text{AFM}} - E_{\text{FM}} = JNZ \langle S \rangle^2, \quad (13)$$

where N is the total number of magnetic moments, S is the spin on each site, and Z is the coordination number. The in-plane interactions within the Cu-O planes in La_2CuO_4 are much stronger than the interplanar interactions, so that we can take $Z = 4$. Since we normalize to one formula unit, $N = 1$. Using the total energies for FM and AFM states obtained from our first-principles computations then yields $J = -138$ meV, where spin-orbit coupling is found to further stabilize the AFM state by 2.5 meV [61]. The present estimate of J is in excellent accord with the experimentally determined J value of -133 ± 3 meV [62,63], and represents a substantial improvement over previous Hartree-Fock calculations [13].

VII. MAGNETIC DENSITY AND THE FORM FACTOR

A test of the efficacy of our first-principles modeling is the reproduction of the experimental magnetic form factor [3], since neutrons probe the local, microscopic magnetism in condensed matter systems. The neutron magnetic cross section can be factored into the dynamical spin-correlation function $S(q, \omega)$ and the squared magnitude of the magnetic form factor $|F(q)|^2$, where $F(q)$ probes effects of the magnetization cloud associated with each magnetic scattering center [64]. $F(q)$ in La_2CuO_4 has been assumed to resemble that of atomic Cu^{2+} , with deviations due to covalency being large enough to be observable [3,65] and to give a strong contribution to the exchange coupling [62,63]. We obtain the magnetic

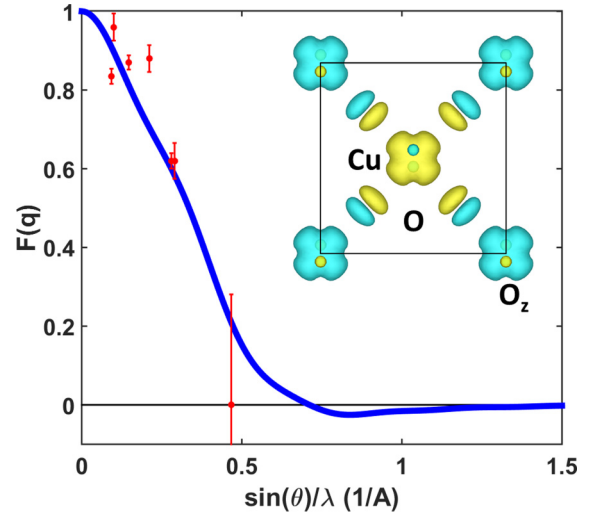


FIG. 6. Theoretical (blue line) and experimental (red dots with error bars, after Ref. [56]) magnetic form factors for the AFM ground state of La_2CuO_4 in the LTO crystal structure. Inset: Spin-density isosurface of the Cu-O plane. Yellow (blue) colors denote positive (negative) spin density; black lines mark the unit cell.

form factor from our spin-dependent charge densities via

$$F(\mathbf{q}) = \int d^3r e^{i\mathbf{k}\cdot\mathbf{r}} \rho_s(\mathbf{r}), \quad (14)$$

by taking the Fourier transform of the spin density $\rho_s(\mathbf{r})$, which is given by $\rho_\uparrow(\mathbf{r}) - \rho_\downarrow(\mathbf{r})$, or the difference of the up- and down-spin densities.

Figure 6 compares the calculated form factor (blue symbols) with the available experimental values [56] (red points). The theoretical $F(q)$, which includes hybridization effects, is seen to be in reasonable accord with the experimental line shape, implying a hybridization strength in accord with experiment. The line shape is similar to that of Walters *et al.* [65], who account for hybridization explicitly in terms of model Wannier functions [66]. Our results yield a significant improvement over previous magnetically constrained studies [67] in which the form factor differed from the atomic and experimental line shapes and predicted a peak between 0.1 and 0.2 \AA^{-1} .

Figure 6 (inset) shows the spin-density isosurface of the Cu-O plane, where yellow (blue) colors denote positive (negative) spin density. The magnetic moment is centered on the copper sites, with the polarization alternating in a checkerboard antiferromagnetic pattern. The magnetic moment is seen to spread from the copper atoms onto the in-plane oxygen atoms through hybridization effects. As a result, the in-plane oxygen atoms develop a spin polarization, wherein the spin-up orbital has, e.g., $s + p_x$ symmetry and the spin-down orbital has $s - p_x$ symmetry, with zero net moment, and the magnetization in the Cu-O plane develops a quadrupole form. Such an effect requires partly filled O orbitals, and hence considerable Cu-O hybridization. The opposing magnetic moment of the apical oxygen atoms is seen above the centers of copper sites.

Further insight is obtained by breaking down the magnetization at various sites into orbital contributions. On copper sites, the moment is dominated by the $d_{x^2-y^2}$ orbital with

$-0.511\mu_B$ with an opposing s contribution of $+0.016\mu_B$. No contributions from the d_{z^2} or the charge saturated t_{2g} manifold were found. The moment on the apical oxygen has mainly a p_z character, with a moment of $+0.008\mu_B$.

VIII. CONCLUDING REMARKS

In conclusion, we have demonstrated clearly that an accurate first-principles treatment of the magnetic structure of the AFM ground state of La_2CuO_4 as an exemplar half-filled high-temperature cuprate superconductor is possible without invoking any free parameters such as the Hubbard U . Our study thus opens a pathway for examining the electronic structures and phase diagrams of cuprates [68] and other complex materials, including magnetic phases, and the evolution of electronic spectra with pressure and doping and the related phenomena.

ACKNOWLEDGMENTS

This work was supported (testing efficacy of new functionals in complex materials) by the DOE Energy Frontier Research Centers: Center for the Computational Design of Functional Layered Materials (DE-SC0012575). The work at Northeastern University was also supported by the (DOE), Office of Science, Basic Energy Sciences (Grant No. DE-FG02-07ER46352) (core research) and benefited from Northeastern University's Advanced Scientific Computation Center, the National Energy Research Scientific Computing Center supercomputing center (DOE Grant No. DE-AC02-05CH11231). The work at Tulane University was also supported by the startup funding from Tulane University. B.B. acknowledges support from the COST Action CA16218.

APPENDIX A: DFT AS A MANY-ELECTRON THEORY AND INTRINSIC LIMITATIONS OF THE BAND THEORY PARADIGM

In the early 1900's the Schrödinger equation for quantum wave functions had already proven highly accurate for simple systems such as He and H_2 , prompting Dirac to declare "chemistry had come to an end—its content was entirely contained in that powerful equation" [18]. However, in almost all practical cases the many-body Schrödinger equation is far too complex to solve. The transformational insight of Kohn [1,2] was to take a different approach by considering the *density* rather than the wave function as the fundamental object for addressing the many-body problem. We emphasize that the density functional theory (DFT) is not designed for obtaining wave functions in its basic construction. DFT is a formally rigorous approach to treat *any* interacting system by mapping it onto a noninteracting system for its ground-state properties [69], and it is thus obviously not a one-electron theory.

The misunderstanding about the DFT being a one-particle theory has been driven in part by the inability of the existing density functionals to describe correctly the ground state of some strongly correlated materials. But, the DFT can, in principle, provide an exact description of the ground state and related physical properties of any material, regardless of the strength of the correlations. The many-body effects are incorporated in the DFT through the treatment of the

exchange-correlation energy (E_{xc}), which in practice must be approximated. We emphasize that even though single-determinant wave functions are invoked prominently in the DFT and give the theory an appearance of being a one-particle theory, these single-determinant wave functions only serve as auxiliary quantities, which provide a natural starting point for incorporating many-body effects in the theory.

The key is to recognize that the DFT maps the interacting many-electron Hamiltonian in a solid onto an effective noninteracting one-electron Hamiltonian, which is rigorously justified insofar as the ground-state energy is concerned. However, the associated one-electron Kohn-Sham energies/orbitals, which are the basis of the common band structures that have come to symbolize band theory so vividly, do not represent the physically relevant quasiparticles of the many-electron system. Even the exact exchange-correlation functional for this reason should not be expected to provide the quasiparticle spectrum of the electron gas. [Notably, time-dependent generalization of the DFT (TDDFT) can, in principle, provide an exact treatment of the excited states.]

Despite the lack of a link with quasiparticles, Kohn-Sham one-particle Bloch states have assumed a commanding air of "reality" over the years and provided an effective basis for coding the essence of the "genome" of a material. The reason is that many experiments, including direct mapping of bands several volts deep in the Fermi sea via angle-resolved photoemission experiments, show clearly that the Bloch states and the related energies and Fermi surfaces predicted by the DFT are in remarkable accord with experiments in wide classes of materials. Such band structures are being used extensively for designing myriad devices for technological applications, and have resulted in the successful prediction of most known topological materials, from insulators to Weyl semimetal phases, before these topological materials were actually realized experimentally [70].

All materials are correlated because electrons confined to lattice dimensions will generally experience quite strong Coulomb forces. The success of the band theory in many materials where the DFT captures measured properties of quasiparticles with remarkable accuracy then suggests that Bloch states in these cases reasonably approximate quasiparticles. It is not unreasonable then to expect that as the description of the ground-state energy improves with the use of improved density functionals, we will also see that the Bloch states better mimic the quasiparticles.

The preceding discussion clearly suggests that the Bloch states produced by SCAN are a better representation of quasiparticles in the cuprates compared to those generated by any other existing density functional. On the other hand, the band theory paradigm as it is practiced currently will never be able to model certain properties of the quasiparticles. For example, the spectral function for Bloch electrons consists of δ functions with uniform spectral weights, but that is not the case in the cuprates where the quasiparticles exhibit finite lifetimes and nonlinear evolutions in spectral weights with doping, and display coherent and incoherent parts in general [14].

Despite the limitations inherent to the band theory framework itself, the ability of the SCAN functional to capture the ground state of LCO and its many key properties opens the door for parameter-free first-principles modeling of electronic

structures of cuprates and other materials that have been considered to be so strongly correlated as to lie outside the scope of the DFT.

APPENDIX B: TECHNICAL ASPECTS OF THE IMPLEMENTATION OF META-GGA EXCHANGE-CORRELATION FUNCTIONALS

The SCAN functional avoids dependence on the density Laplacian in favor of the orbital kinetic energy density in its construction. Moreover, SCAN involves only the orbital kinetic energy density as information beyond the GGA. Although functionals invoking the density Laplacian have generally been taken to belong to the “meta-GGA” classification, the orbital kinetic energy density is the more commonly accepted ingredient in meta-GGA functionals. We employ the method of Handy’s group [71] in which the total energy is minimized with respect to the occupied orbitals and yields an effective orbital-dependent potential. The technique of partial integration is further employed in VASP to avoid requiring higher-order derivatives of the basis set. These techniques are also summarized in Ref. [72].

Numerically, the SCAN functional is sensitive to real-space grid density [73]. We have thoroughly checked the convergence of all our results with respect to grid densities. Notably, the sensitivity of the SCAN functional to the grid density reflects the presence of fine structure in the potential, and not the use of high-order derivatives. As we sample diverse chemical environments in a crystal, the SCAN potential undergoes dramatic changes as it attempts to accommodate rapid variations in the types of bondings involved, especially in the intershell regions. This in turn drives fine structures in the SCAN potential.

TABLE II. Theoretical and experimental lattice parameters, volume, and Wyckoff positions for atomic sites in the low-temperature orthorhombic (LTO) phase of La_2CuO_4 . The calculated structural data are in agreement with the $Bmab$ symmetry found experimentally.

		Experiment ^a	Present theory
a (Å)		5.3350	5.324
b (Å)		5.4209	5.458
c (Å)		13.1068	13.087
V (Å ³)		379.0552	380.313
La	x	0	0
	y	0.0092	0.0117
	z	0.3618	0.3608
Cu	$x = y = z$	0	0
	O(1)	$x = y$	0.25
O(2)	z	0.0085	0.0113
	x	0	0
	y	-0.0426	-0.0562
Octahedral tilt (deg) ^b	z	0.1839	0.1858
	O(1)	3.3532	4.4538
	O(2)	5.4727	7.1971

^aExperimental structural data are taken from Ref. [32] as stated in Ref. [33].

^bThe tilt angle is measured off of the ab plane and the c axis for O(1) and O(2), respectively. The calculated tilt angles are consistent with the results of Refs. [74,75].

APPENDIX C: DETAILS OF CRYSTAL STRUCTURE

Details of the crystal structure are given in Table II.

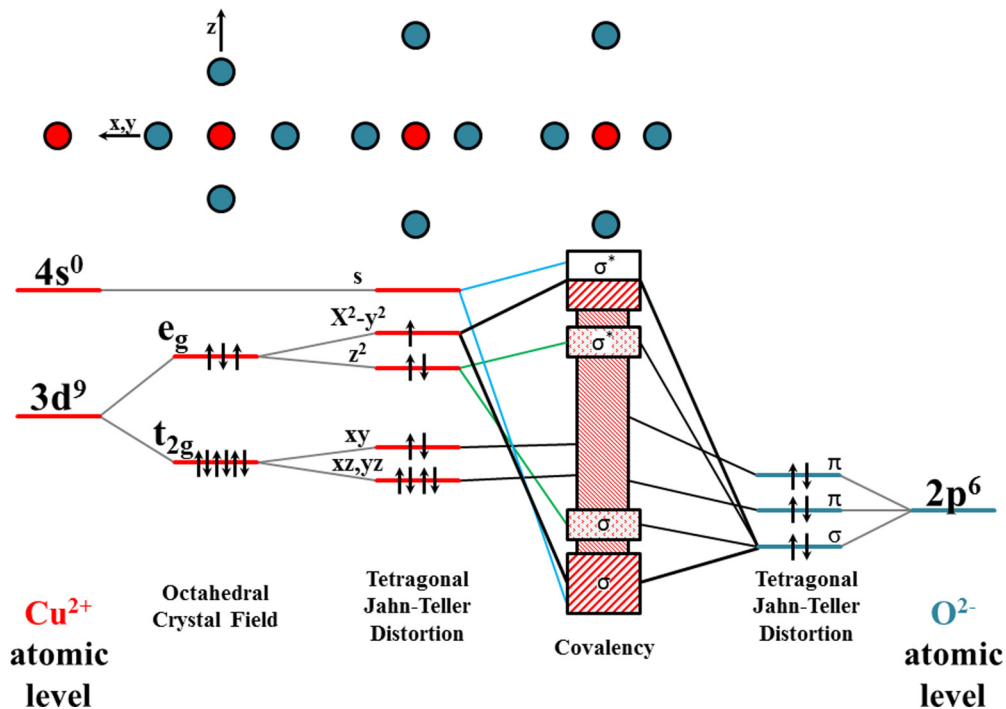


FIG. 7. The schematic molecular-bonding picture of octahedrally coordinated Cu discussed in the text.

APPENDIX D: MOLECULAR-BONDING PICTURE OF OCTAHEDRALLY COORDINATED Cu IN La_2CuO_4

Figure 7 shows a schematic of the molecular-bonding picture of octahedrally coordinated Cu in La_2CuO_4 , which is adapted from that presented in Refs. [36,37]. A sketch of the atomic positions is given in the top portion of the figure, where Cu and O atoms are shown in red and teal colors, respectively. The atomic Cu $3d$ levels in an octahedral crystal field split into e_g and t_{2g} manifolds. A tetragonal Jahn-Teller distortion splits the e_g and t_{2g} states along with the O $2p$ states, as shown. In the central portion of the figure, we show the resulting hybridized complex of states, along with the separation of the bonding (σ) and antibonding (σ^*) states for $d_{x^2-y^2}$ and d_{z^2} orbitals. The d_{z^2} bonding and antibonding states have been included due to their sizable contribution to the valence states in the AFM phase as discussed in the main text.

APPENDIX E: EXPERIMENTAL COPPER MAGNETIC MOMENTS

Table III compares copper magnetic moments from various experiments, including the value given in the recent review of Tranquada [53]. The considerable variability in the values stems from variations in sample quality and the approximate nature of the form factors used in calculating the copper magnetic moment. We hope that our first-principles form

TABLE III. Experimental copper magnetic moments of AFM La_2CuO_4 obtained via neutron scattering measurements. The magnetic form factor used in calculating the magnetic moment is indicated in those cases where it is available.

Experimental technique	Cu magnetic moment (μ_B)	Reference	Form factor
Powder	0.48 ± 0.15	[76]	$f(Q) = 0.75$ (K_2CuF_4) [77]
Powder	0.4	[76]	Cu^{++}
Powder	0.43 ± 0.13	[78]	$f(Q) = 0.75$ (K_2CuF_4) [77]
Single crystal	0.35 ± 0.05	[79]	N/A
Single crystal	0.60 ± 0.05	[54]	$f(100) = 0.835$ (K_2CuF_4) [80]
Single crystal	0.30	[56]	$f(100) = 0.835$ (K_2CuF_4) [80]
Single crystal	0.40	[75]	N/A

factor presented in this study will aid in obtaining improved experimental magnetic moment values.

APPENDIX F: NM AND AFM BAND STRUCTURES AND THEIR ORBITAL PROJECTIONS

Figures 8–15 give band structures (blue lines) of La_2CuO_4 in the LTO crystal structure for the nonmagnetic (NM) and antiferromagnetic (AFM) states overlaid with various site-resolved atomic projections (red dots).

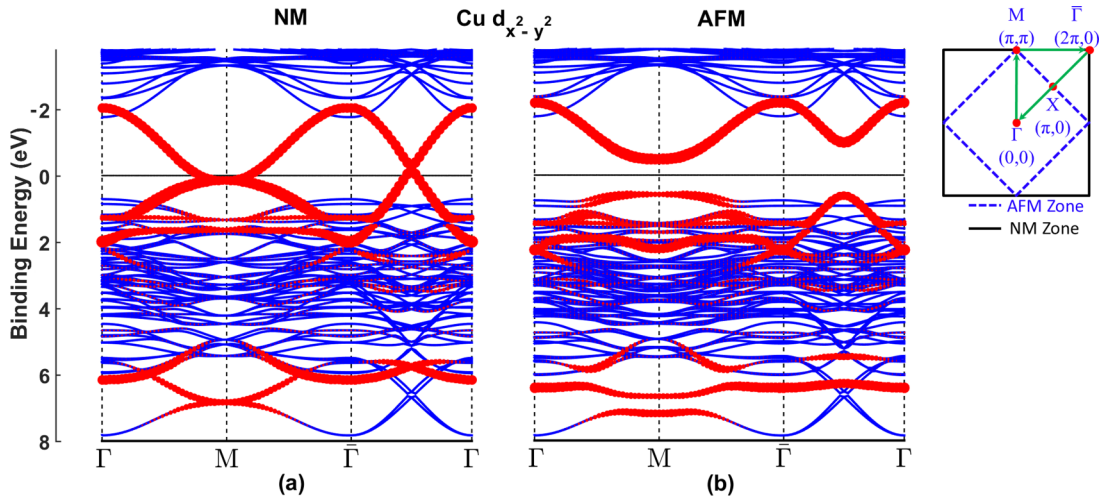


FIG. 8. Band structures (blue lines) along the high-symmetry lines in the Brillouin zone in the NM and AFM phases of La_2CuO_4 in the LTO crystal structure. Contribution of Cu $d_{x^2-y^2}$ orbitals is highlighted with red dots. The sizes of the red dots are proportional to the fractional weights of the Cu $d_{x^2-y^2}$ orbital in the corresponding crystal wave functions. A schematic diagram of the NM and AFM Brillouin zones with the path followed in presenting the band structures is shown on the right.

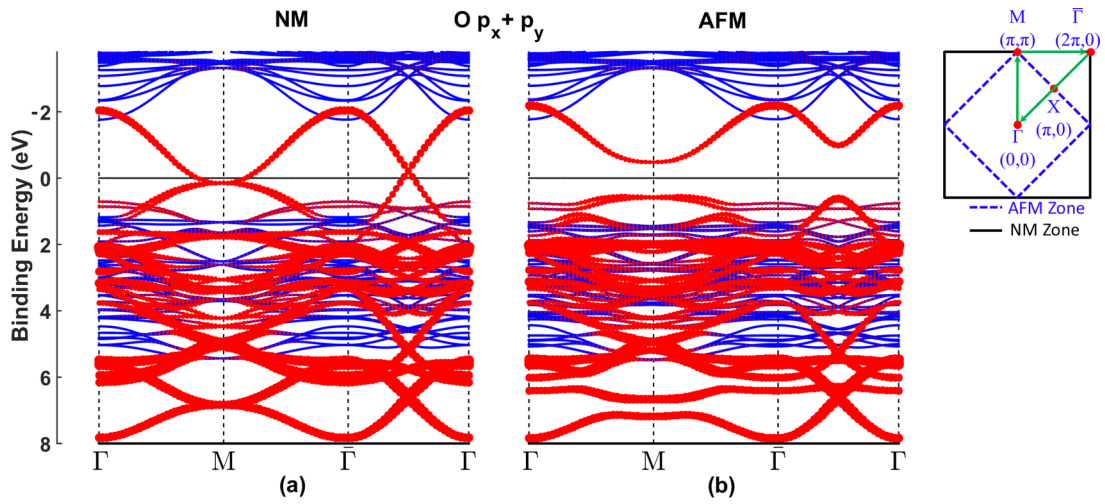


FIG. 9. Same as the caption to Fig. 8, except that this figure refers to O $p_x + p_y$ orbital contributions to the band structures.

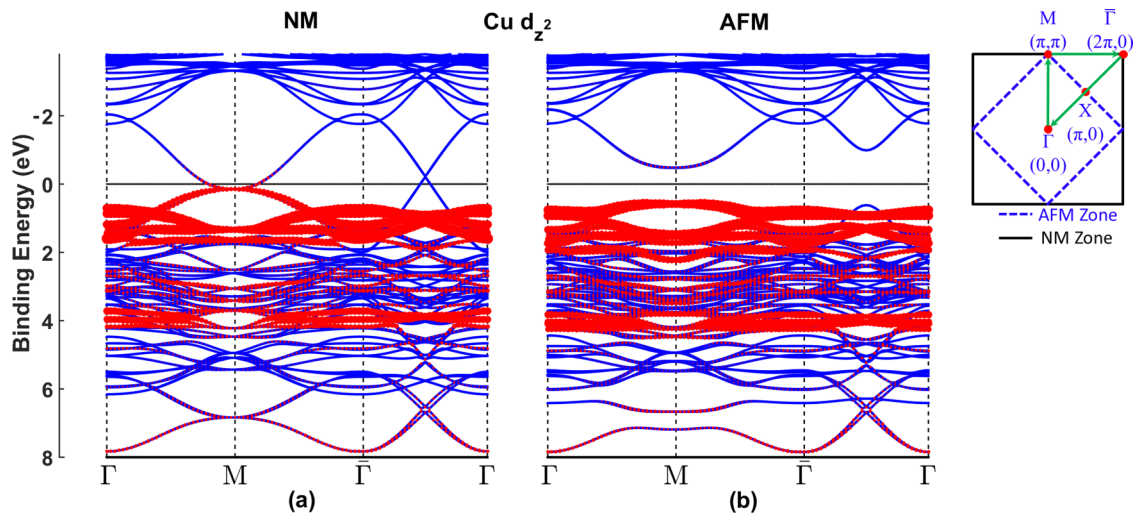


FIG. 10. Same as the caption to Fig. 8, except that this figure refers to Cu d_{z^2} orbital contributions to the band structures.

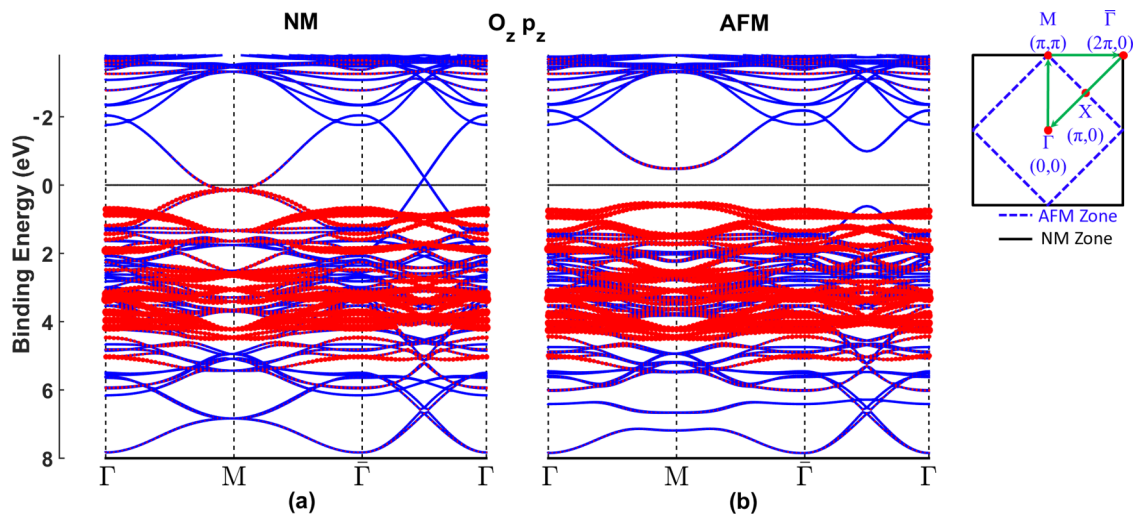


FIG. 11. Same as the caption to Fig. 8, except that this figure refers to O $_z p_z$ orbital contributions to the band structures.

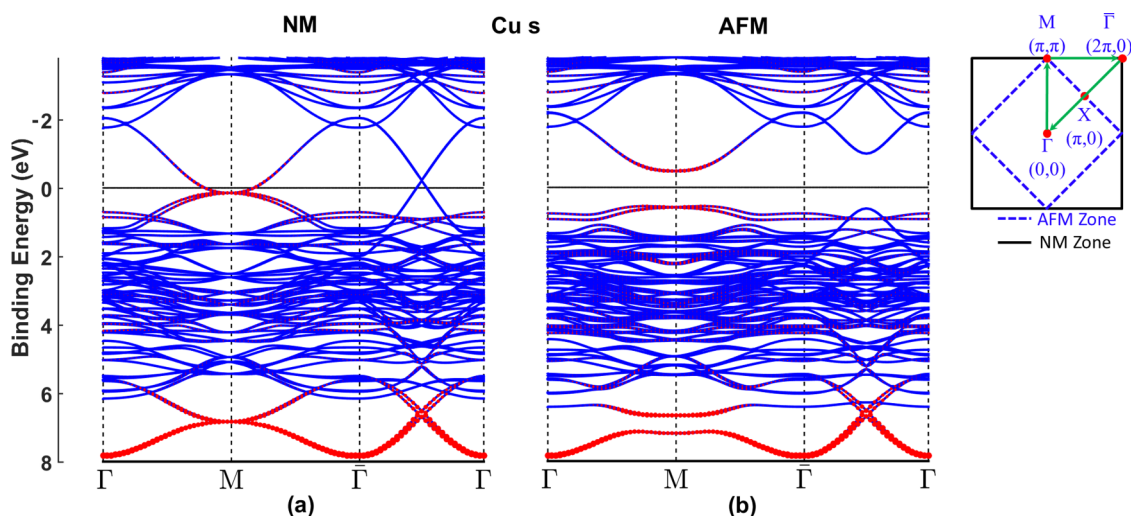


FIG. 12. Same as the caption to Fig. 8, except that this figure refers to Cu s orbital contributions to the band structures.

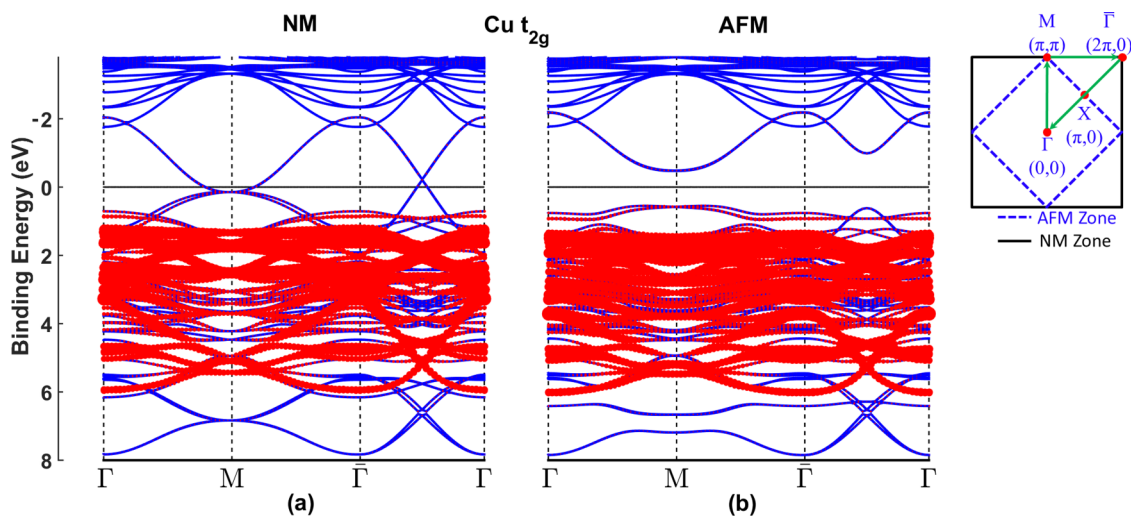


FIG. 13. Same as the caption to Fig. 8, except that this figure refers to Cu t_{2g} orbital contributions to the band structures.

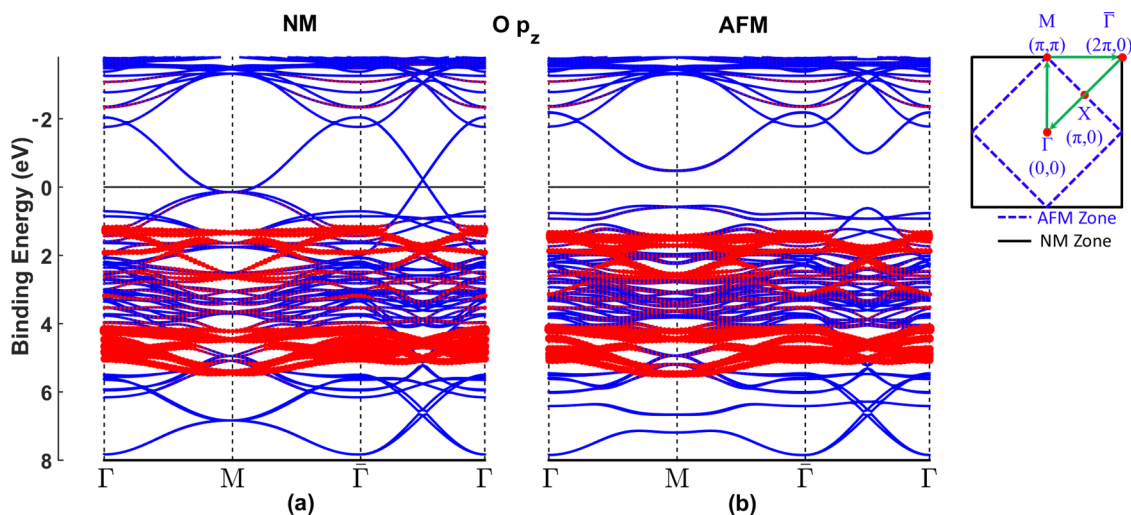


FIG. 14. Same as the caption to Fig. 8, except that this figure refers to O p_z orbital contributions to the band structures.

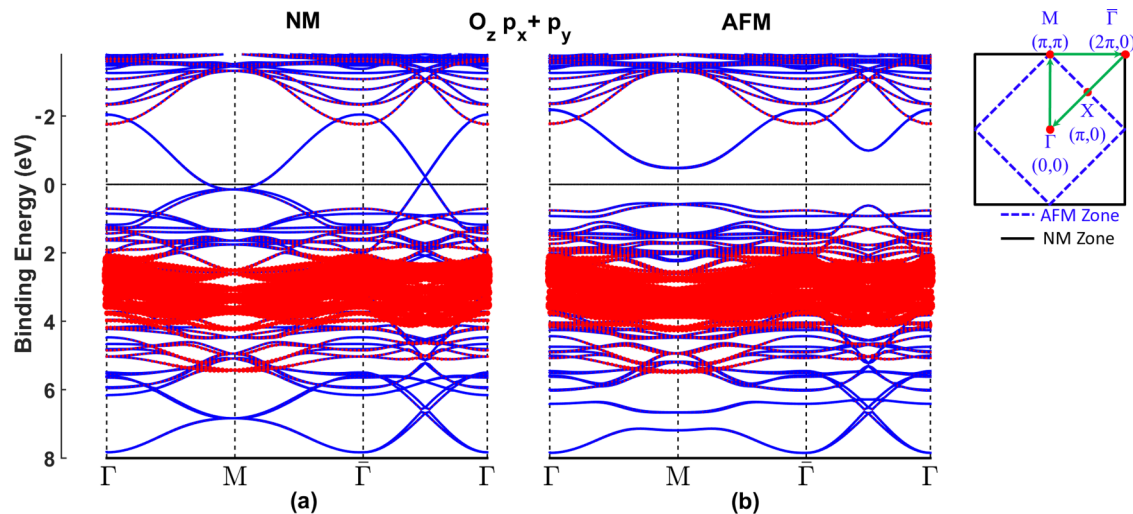


FIG. 15. Same as the caption to Fig. 8, except that this figure refers to $O_z p_x + p_y$ orbital contributions to the band structures.

- [1] P. Hohenberg and W. Kohn, *Phys. Rev.* **136**, B864 (1964).
- [2] W. Kohn and L. J. Sham, *Phys. Rev.* **140**, A1133 (1965).
- [3] W. E. Pickett, *Rev. Mod. Phys.* **61**, 433 (1989).
- [4] R. O. Jones and O. Gunnarsson, *Rev. Mod. Phys.* **61**, 689 (1989).
- [5] J. P. Perdew and A. Zunger, *Phys. Rev. B* **23**, 5048 (1981).
- [6] J. Yu, A. J. Freeman, and J. H. Xu, *Phys. Rev. Lett.* **58**, 1035 (1987).
- [7] L. F. Mattheiss, *Phys. Rev. Lett.* **58**, 1028 (1987).
- [8] C. Ambrosch-Draxl and K. Schwarz, *Solid State Commun.* **77**, 45 (1991).
- [9] J. P. Perdew, K. Burke, and M. Ernzerhof, *Phys. Rev. Lett.* **77**, 3865 (1996).
- [10] D. J. Singh and W. E. Pickett, *Phys. Rev. B* **44**, 7715 (1991).
- [11] S. Uchida, T. Ido, H. Takagi, T. Arima, Y. Tokura, and S. Tajima, *Phys. Rev. B* **43**, 7942 (1991).
- [12] S. Ono, S. Komiya, and Y. Ando, *Phys. Rev. B* **75**, 024515 (2007).
- [13] Y.-S. Su, T. A. Kaplan, S. D. Mahanti, and J. F. Harrison, *Phys. Rev. B* **59**, 10521 (1999).
- [14] T. Das, R. S. Markiewicz, and A. Bansil, *Adv. Phys.* **63**, 151 (2014).
- [15] G. Kotliar, S. Y. Savrasov, K. Haule, V. S. Oudovenko, O. Parcollet, and C. A. Marianetti, *Rev. Mod. Phys.* **78**, 865 (2006).
- [16] K. Held, I. A. Nekrasov, G. Keller, V. Eyert, N. Blümer, A. K. McMahan, R. T. Scalettar, T. Pruschke, V. I. Anisimov, and D. Vollhardt, *Phys. Status Solidi B* **243**, 2599 (2006).
- [17] H. Park, K. Haule, and G. Kotliar, *Phys. Rev. Lett.* **101**, 186403 (2008).
- [18] W. Kohn, *Rev. Mod. Phys.* **71**, 1253 (1999).
- [19] See Appendix A for further discussion.
- [20] J. Sun, A. Ruzsinszky, and J. P. Perdew, *Phys. Rev. Lett.* **115**, 036402 (2015).
- [21] For technical implementation aspects of meta-GGA functionals, see Appendix B.
- [22] R. Car, *Nat. Chem.* **8**, 820 (2016).
- [23] A. Patra, J. E. Bates, J. Sun, and J. P. Perdew, *Proc. Natl. Acad. Sci. USA* **114**, E9188 (2017).
- [24] J. Sun, R. C. Remsing, Y. Zhang, Z. Sun, A. Ruzsinszky, H. Peng, Z. Yang, A. Paul, U. Waghmare, X. Wu *et al.*, *Nat. Chem.* **8**, 831 (2016).
- [25] M. Chen, H.-Y. Ko, R. C. Remsing, M. F. C. Andrade, B. Santra, Z. Sun, A. Selloni, R. Car, M. L. Klein, J. P. Perdew *et al.*, *Proc. Natl. Acad. Sci. USA* **114**, 10846 (2017).
- [26] A. Paul, J. Sun, J. P. Perdew, and U. V. Waghmare, *Phys. Rev. B* **95**, 054111 (2017).
- [27] Y. Zhang, J. Sun, J. P. Perdew, and X. Wu, *Phys. Rev. B* **96**, 035143 (2017).
- [28] J. W. Furness, Y. Zhang, C. Lane, I. G. Buda, B. Barbiellini, R. S. Markiewicz, A. Bansil, and J. Sun, *Commun. Phys.* **1**, 11 (2018).
- [29] G. Kresse and D. Joubert, *Phys. Rev. B* **59**, 1758 (1999).
- [30] G. Kresse and J. Furthmüller, *Phys. Rev. B* **54**, 11169 (1996).
- [31] G. Kresse and J. Hafner, *Phys. Rev. B* **48**, 13115 (1993).
- [32] J. D. Jorgensen, B. Dabrowski, S. Pei, D. G. Hinks, L. Soderholm, B. Morosin, J. E. Schirber, E. L. Venturini, and D. S. Ginley, *Phys. Rev. B* **38**, 11337 (1988).
- [33] D. M. Ginsberg, *Physical Properties of High Temperature Superconductors II* (World Scientific, Singapore, 1998).
- [34] The energy of the NM state is 0.593 eV/unit cell higher than that of the AFM state. For this reason, this state is not relevant for low-energy physics. Moreover, our preliminary results on $\text{YBa}_2\text{Cu}_3\text{O}_{7-\delta}$ (YBCO) show that the NM state is not relevant in the pristine or the doped phase. Here, the NM state is shown only for the purpose of comparison.
- [35] J. Goodenough, *Magnetism and the Chemical Bond* (Interscience, New York, 1963).
- [36] C. Rao and B. Raveau, *Transition Metal Oxides: Structure, Properties, and Synthesis of Ceramic Oxides* (Wiley, New York, 1998).
- [37] J. Fink, N. Nucker, H. Romberg, and J. Fuggle, *IBM J. Res. Dev.* **33**, 372 (1989).
- [38] C. Ye, P. Cai, R. Yu, X. Zhou, W. Ruan, Q. Liu, C. Jin, and Y. Wang, *Nat. Commun.* **4**, 1365 (2013).
- [39] We have carried out modeling of the optical spectra of the cuprates, and shown that the computed spectrum reasonably

- reproduces the measured spectrum in the half-filled cuprates with a leading edge gap of about 1 eV; see Ref. [81] for details.
- [40] J. P. Perdew, W. Yang, K. Burke, Z. Yang, E. K. Gross, M. Scheffler, G. E. Scuseria, T. M. Henderson, I. Y. Zhang, A. Ruzsinszky *et al.*, *Proc. Natl. Acad. Sci. USA* **114**, 2801 (2017).
- [41] Y. Zhao and D. G. Truhlar, *J. Chem. Phys.* **125**, 194101 (2006).
- [42] J. Tao, J. P. Perdew, V. N. Staroverov, and G. E. Scuseria, *Phys. Rev. Lett.* **91**, 146401 (2003).
- [43] J. P. Perdew, A. Ruzsinszky, G. I. Csonka, L. A. Constantin, and J. Sun, *Phys. Rev. Lett.* **103**, 026403 (2009).
- [44] J. Sun, B. Xiao, Y. Fang, R. Haunschild, P. Hao, A. Ruzsinszky, G. I. Csonka, G. E. Scuseria, and J. P. Perdew, *Phys. Rev. Lett.* **111**, 106401 (2013).
- [45] Y. Sakurai, M. Itou, B. Barbiellini, P. Mijnders, R. Markiewicz, S. Kaprzyk, J.-M. Gillet, S. Wakimoto, M. Fujita, S. Basak *et al.*, *Science* **332**, 698 (2011).
- [46] J. Zaanen, G. A. Sawatzky, and J. W. Allen, *Phys. Rev. Lett.* **55**, 418 (1985).
- [47] A. Oleś, *Phys. Rev. B* **28**, 327 (1983).
- [48] Note, in the AFM unit cell the projected d_{yz} and d_{xz} orbitals do not align along the Cu-O bond and should be considered a linear combination of their aligned counterparts. However, this basis-set effect is averaged out and we find the same average spin splitting.
- [49] S. W. Jang, H. Sakakibara, H. Kino, T. Kotani, K. Kuroki, and M. J. Han, *Sci. Rep.* **6**, 33397 (2016).
- [50] A. Comanac, L. de'Medici, M. Capone, and A. Millis, *Nat. Phys.* **4**, 287 (2008).
- [51] A. Paramekanti and J. B. Marston, *J. Phys.: Condens. Matter* **19**, 125215 (2007).
- [52] The local magnetic moment of $0.495\mu_B$ is calculated by integrating the magnetic moment within a PAW sphere of radius 2.20 Å.
- [53] J. M. Tranquada, in *Handbook of High-Temperature Superconductivity* (Springer, Berlin, 2007), pp. 257–298.
- [54] K. Yamada, E. Kudo, Y. Endoh, Y. Hidaka, M. Oda, M. Suzuki, and T. Murakami, *Solid State Commun.* **64**, 753 (1987).
- [55] M. A. Kastner, R. J. Birgeneau, G. Shirane, and Y. Endoh, *Rev. Mod. Phys.* **70**, 897 (1998).
- [56] T. Freltoft, G. Shirane, S. Mitsuda, J. P. Remeika, and A. S. Cooper, *Phys. Rev. B* **37**, 137 (1988).
- [57] Since the low-temperature spins in LCO are experimentally seen to be Ising-like, we expect to reasonably capture fluctuation effects in our computed moments.
- [58] Our value of the moment is in good agreement with QMC calculations [82], although our model goes a step beyond these calculations by including the spin-orbit pinning of the moment to the lattice.
- [59] *High-Temperature Superconductivity*, edited by K. Bedell, D. Coffey, D. Meltzer, D. Pines, and J. Schrieffer (Addison-Wesley, Redwood City, CA, 1990).
- [60] L. Noodleman, *J. Chem. Phys.* **74**, 5737 (1981).
- [61] We expect that a direct first-principles computation of the charge and magnetic susceptibilities of our AFM ground state of La_2CuO_4 will reproduce the spin-wave spectrum reasonably, as was demonstrated by Savrasov [83] and from tight-binding fits to LDA within many-body perturbation theory [84,85].
- [62] P. Bourges, H. Casalta, A. S. Ivanov, and D. Petitgrand, *Phys. Rev. Lett.* **79**, 4906 (1997).
- [63] R. Coldea, S. M. Hayden, G. Aeppli, T. G. Perring, C. D. Frost, T. E. Mason, S.-W. Cheong, and Z. Fisk, *Phys. Rev. Lett.* **86**, 5377 (2001).
- [64] A. Furrer, T. Strassle, and J. Mesot, *Neutron Scattering in Condensed Matter Physics*, Series on Neutron Techniques and Applications (World Scientific, Singapore, 2009).
- [65] A. C. Walters, T. G. Perring, J.-S. Caux, A. T. Savici, G. D. Gu, C.-C. Lee, W. Ku, and I. A. Zaliznyak, *Nat. Phys.* **5**, 867 (2009).
- [66] Notably, we do not *a priori* assume the orbital character for the density used in calculating the magnetic form factor as was done by Walters *et al.* [65]. By using our self-consistent magnetic density, we automatically include contributions from orbitals beyond Cu $d_{x^2-y^2}$ and O p_x, p_y .
- [67] T. C. Leung, X. W. Wang, and B. N. Harmon, *Phys. Rev. B* **37**, 384 (1988).
- [68] Our preliminary results using SCAN on YBCO, Hg compounds, and Tl cuprates also indicate that the SCAN functional stabilizes the AFM ground state of the half-filled systems.
- [69] K. Burke *et al.*, *The ABC of DFT* (Department of Chemistry, University of California - Irvine 2007), p. 40.
- [70] A. Bansil, H. Lin, and T. Das, *Rev. Mod. Phys.* **88**, 021004 (2016).
- [71] R. Neumann, R. H. Nobes, and N. C. Handy, *Mol. Phys.* **87**, 1 (1996).
- [72] J. Sun, M. Marsman, G. I. Csonka, A. Ruzsinszky, P. Hao, Y.-S. Kim, G. Kresse, and J. P. Perdew, *Phys. Rev. B* **84**, 035117 (2011).
- [73] Z.-h. Yang, H. Peng, J. Sun, and J. P. Perdew, *Phys. Rev. B* **93**, 205205 (2016).
- [74] E. S. Bozin, R. Zhong, K. R. Knox, G. Gu, J. P. Hill, J. M. Tranquada, and S. J. L. Billinge, *Phys. Rev. B* **91**, 054521 (2015).
- [75] K. Yamada, K. Kakurai, Y. Endoh, T. R. Thurston, M. A. Kastner, R. J. Birgeneau, G. Shirane, Y. Hidaka, and T. Murakami, *Phys. Rev. B* **40**, 4557 (1989).
- [76] D. Vaknin, S. K. Sinha, D. E. Moncton, D. C. Johnston, J. M. Newsam, C. R. Safinya, and H. E. King, *Phys. Rev. Lett.* **58**, 2802 (1987).
- [77] K. Hirakawa and H. Ikeda, *Phys. Rev. Lett.* **33**, 374 (1974).
- [78] S. Mitsuda, G. Shirane, S. K. Sinha, D. C. Johnston, M. S. Alvarez, D. Vaknin, and D. E. Moncton, *Phys. Rev. B* **36**, 822(R) (1987).
- [79] G. Shirane, Y. Endoh, R. J. Birgeneau, M. A. Kastner, Y. Hidaka, M. Oda, M. Suzuki, and T. Murakami, *Phys. Rev. Lett.* **59**, 1613 (1987).
- [80] J. Akimitsu and Y. Ito, *J. Phys. Soc. Jpn.* **40**, 1621 (1976).
- [81] T. Das, R. S. Markiewicz, and A. Bansil, *Phys. Rev. B* **81**, 174504 (2010).
- [82] L. K. Wagner and P. Abbamonte, *Phys. Rev. B* **90**, 125129 (2014).
- [83] S. Y. Savrasov, *Phys. Rev. Lett.* **81**, 2570 (1998).
- [84] J. R. Schrieffer, X.-G. Wen, and S.-C. Zhang, *Phys. Rev. Lett.* **60**, 944 (1988).
- [85] A. Singh and Z. Tešanović, *Phys. Rev. B* **41**, 614 (1990).